The MUSE-Wide survey: a measurement of the Ly α emitting fraction among z > 3 galaxies

Joseph Caruana, Lutz Wisotzki, Edmund Christian Herenz, Josephine Kerutt, Tanya Urrutia, Kasper Borello Schmidt, Rychard Bouwens, Jarle Brinchmann, Sebastiano Cantalupo, Marcella Carollo, et al.

Monthly Notices of the ROYAL ASTRONOMICAL SOCIETY

MNRAS **473,** 30–37 (2018) doi:10.1093/mnras/stx2307
Advance Access publication 2017 September 6

The MUSE-Wide survey: a measurement of the Ly α emitting fraction among $z > 3$ galaxies

Joseph Caruana,[1,2,3]★ Lutz Wisotzki,[3] Edmund Christian Herenz,[4] Josephine Kerutt,[3] Tanya Urrutia,[3] Kasper Borello Schmidt,[3] Rychard Bouwens,[5] Jarle Brinchmann,[5,6] Sebastiano Cantalupo,[7] Marcella Carollo,[7] Catrina Diener,[8] Alyssa Drake,[9] Thibault Garel,[9] Raffaella Anna Marino,[7] Johan Richard,[9] Rikke Saust,[3] Joop Schaye[5] and Anne Verhamme[9]

[1]*Department of Physics, University of Malta, Msida MSD 2080, Malta*
[2]*Institute for Space Sciences & Astronomy, University of Malta, Msida MSD 2080, Malta*
[3]*Leibniz Institut für Astrophysik, An der Sternwarte 16, D-14482 Potsdam, Germany*
[4]*Department of Astronomy, Stockholm University, AlbaNova University Centre, SE-106 91 Stockholm, Sweden*
[5]*Leiden Observatory, Leiden University, PO Box 9513, NL-2300 RA, Leiden, the Netherlands*
[6]*Instituto de Astrofísica e Ciências do Espaço, Universidade do Porto, CAUP, Rua das Estrelas, P-4150-762 Porto, Portugal*
[7]*ETH Zurich, Institute for Astronomy, HIT J31.5, Wolfgang-Pauli-Strasse 27, CH-8093 Zurich, Switzerland*
[8]*Institute of Astronomy, Madingley Road, Cambridge CB3 0HA, UK*
[9]*Univ Lyon, Univ Lyon1, Ens de Lyon, CNRS, Centre de Recherche Astrophysique de Lyon UMR5574, F-69230 Saint-Genis-Laval, France*

Accepted 2017 September 4. Received 2017 September 4; in original form 2017 June 17

ABSTRACT

We present a measurement of the fraction of Lyman α (Ly α) emitters ($X_{\mathrm{Ly}\,\alpha}$) amongst *HST* continuum-selected galaxies at $3 < z < 6$ with the Multi-Unit Spectroscopic Explorer (MUSE) on the VLT. Making use of the first 24 MUSE-Wide pointings in GOODS-South, each having an integration time of 1 h, we detect 100 Ly α emitters and find $X_{\mathrm{Ly}\,\alpha} \gtrsim 0.5$ for most of the redshift range covered, with 29 per cent of the Ly α sample exhibiting rest equivalent widths (rest-EWs) ≤ 15 Å. Adopting a range of rest-EW cuts (0–75 Å), we find no evidence of a dependence of $X_{\mathrm{Ly}\,\alpha}$ on either redshift or ultraviolet luminosity.

Key words: galaxies: high-redshift – galaxies: star formation – galaxies: statistics.

1 INTRODUCTION

Lyman α (Ly α) emitters have been the subject of a large number of studies over the past several years. The Ly α line often being the strongest emission line in the ultraviolet (UV) for star-forming galaxies (see, e.g. Peebles & Partridge 1967; Amorín et al. 2017), it holds the answer to several pieces of information, most crucially the determination of the galaxies' redshift. Key questions about these objects revolve around their masses, ages and dust extinction – and their relationship to continuum selected galaxies, particularly the extent to which such galaxies exhibit this emission line. The fraction of Ly α emitters amongst continuum-detected sources, the Ly α emitter fraction, $X_{\mathrm{Ly}\,\alpha}$, is related to the underlying distribution of Ly α equivalent widths (EWs) amongst these objects, thus yielding additional information to that provided by Ly α emitter luminosity functions. In recent years, the evolution of the Ly α fraction with redshift has also seen widespread use in probing the neutral HI fraction of the intergalactic medium at $z > 6$ (e.g. Pentericci et al. 2011; Caruana et al. 2012; Ono et al. 2012; Schenker et al. 2012; Caruana et al. 2014), making accurate measurements of $X_{\mathrm{Ly}\,\alpha}$ at lower redshifts crucial. The measurement of $X_{\mathrm{Ly}\,\alpha}$ also provides a point of reference for theoretical approaches that use it as an observational assessment of galaxy evolution and reionization models (e.g. Dayal, Maselli & Ferrara 2011; Forero-Romero et al. 2011; Garel et al. 2015; Garel, Guideroni & Blaizot 2016; Kakiichi et al. 2016; for a review, see Dijkstra, 2014) with some models failing to reproduce aspects of the Lyα emitter population such as high EW (>100 Å) emitters.

A better understanding of the nature of Ly α emitters requires homogeneous, statistically-significant surveys of these objects. Several studies have been conducted in this vein, mostly employing multiobject spectrosopy (e.g. Stark et al. 2010; Mallery et al. 2012; Cassata et al. 2015) and narrow-band imaging (e.g. Rhoads et al. 2000; Ouchi et al. 2008). Both of these approaches carry their own respective drawbacks. Multiobject slit spectroscopy often entails choosing an observing setup that is configured (e.g. via the choice of an appropriate grism) to target the required wavelength space. This, in turn, requires a pre-selected catalogue of sources whose probable redshift range has already been estimated

★ E-mail: joseph.caruana@um.edu.mt

(e.g. via photometric selection). Moreover, the slit geometry can pose problems and necessitate compromises (e.g. with overlapping slits in the case of objects in spatial proximity) and the spectra themselves are prone to slit losses. Finally, skyline contamination can be a greater problem compared to narrow-band searches. On the other hand, in the case of narrow-band imaging, the setup is tuned to a specific redshift, meaning that this approach is more suited to surveying a narrow redshift slice. Furthermore, the sensitivity can be lower than in the case of slit spectroscopy (by virtue of the filter width being wider than the spectral extent of the Ly α emission line).

The ESO-VLT Multi Unit Spectroscopic Explorer (MUSE, Bacon et al. 2010) is an integral field spectrograph that offers both high spatial resolution (0.2 × 0.2 arcsec) and a wide spectral range from 4750 to 9300 Å. This wide wavelength coverage translates into a possibility to investigate Ly α over a wide redshift range spanning $z = 2.91$–6.64, which was one of the principal scientific drivers for the construction of the instrument. Being an IFU imager/spectrograph, it does away with the requirement to set up multiple slits with associated flux losses. These advantages together with its high throughput and wide field of view (1 arcmin^2) make MUSE an optimal instrument for Ly α surveys.

In this study, we present results from MUSE-Wide, a relatively shallow survey with MUSE, taken as part of Guaranteed Time Observations (GTO). Basing on *HST* imaging catalogues (Guo et al. 2013; Skelton et al. 2014) for GOODS South, our study focuses on objects that are continuum-bright ($m_{775W} < 26.5$), and survey for relatively bright emission line galaxies with the emphasis lying on wide-area coverage whilst employing relatively short integration times. This approach enables us to straightforwardly determine the redshift for all sources that exhibit Ly α. We investigate $X_{\mathrm{Ly}\,\alpha}$ and its relation to UV luminosity and redshift, and derive EW measurements for all emitters in our sample, which include a number of objects exhibiting very low (sub-10 Å) EWs. Our results demonstrate the benefit of employing IFU spectroscopy combined with optimal spectral extraction (detailed in Section 3.2), which allows us to better capture the flux from sources that would otherwise go undetected. This suggests that current estimates of the Ly α fraction might be underestimating the number of Ly α emitters, and by extension, inferences on the evolution of this fraction both with redshift and M_{UV} should be considered with caution.

In this paper, we adopt a Λcold dark matter cosmology throughout, with $\Omega_M = 0.3$, $\Omega_\Lambda = 0.7$ and $H_0 = 70\,\mathrm{km\,s^{-1}\,Mpc^{-1}}$. Magnitudes are given in the AB system (Oke & Gunn 1983).

2 OBSERVATIONS AND DATA PROCESSING

The MUSE-Wide project (see also Herenz et al. 2017) is a blind spectroscopic survey (PI: L. Wisotzki) using the MUSE panoramic integral field spectrograph at the ESO-VLT, carried out as a part of the GTO awarded to the MUSE consortium. The final survey covers some 100 arcmin^2 in areas with deep *HST* imaging and complementary multiwavelength data, with the *Chandra Deep Field*-South (CDFS) as the primary region of interest. MUSE covers a fixed spectral range from 4750 to 9300 Å with a resolution of 2.5Å (full width at half-maximum).

This paper uses data from the first 24 MUSE-Wide pointings in the CDFS-Deep part of the CANDELS *HST* imaging survey (Cosmic Assembly Near-Infrared Deep Extragalactic Legacy Survey; Grogin et al. 2011, Koekemoer et al. 2011), which in turn was built on top of the earlier GOODS imaging campaign (Giavalisco et al. 2004). Our 24 MUSE fields are also all located within the footprint of the 3D-HST grism survey (Brammer et al. 2012; Momcheva et al. 2016).

A detailed account of the observations, calibration and data reduction procedures will be given in a forthcoming publication (Urrutia et al., in preparation) accompanying the first data release of MUSE-Wide. In brief, all calibration exposures followed the ESO calibration plan. For the data reduction, we used the MUSE data reduction pipeline (v1.0) with custom enhancements of the flat fielding and sky subtraction steps. After processing each single exposure separately and converting it into a data cube on a predefined world coordinate system grid, the four 900 s exposures of one pointing were co-added into a final single data cube. These 24 data cubes, one for each MUSE pointing in the CDFS, were the basis of all further analysis.

3 ANALYSIS

3.1 Catalogues of *HST* continuum-detected sources

The CANDELS team produced a catalogue of all detected continuum sources in GOODS South (Guo et al. 2013). We made use of this catalogue for the purpose of our study, applying a magnitude-cut to select all sources from this catalogue that satisfied $m_{775W} < 26.5$. Since the CANDELS/3D-HST near-infrared-detected catalogue by Skelton et al. (2014) also includes photometric redshifts, we cross-matched the Guo et al. (2013) catalogue to that of Skelton et al. (2014); this allowed us to also apply a photometric-redshift cut to our selection. We adopted a conservative cut and selected those sources that satisfied $z_{\mathrm{phot}} > 2$. Such a low z_{phot} threshold (Ly α enters the MUSE spectral range only at $z > 2.9$) was adopted in order to minimize the number of sources, which potentially had a larger error on their photometric redshift. At the same time, this choice sped up our analysis considerably by greatly cutting down on the number of sources whose spectra had to be subsequently inspected for Ly α. These selection criteria resulted in a list of 579 sources, revised to 532 following the removal of 47 objects that lay close to the edge of the MUSE field-of-view. To define 'edge-objects', for each source, we considered the cube layer at which Ly α peaked (or, if no emission line was visible, would be expected to peak basing upon z_{phot}) and checked whether there was any pixel within a spatial radius of 13 pixels (in that layer), which had less than two exposure cubes contributing to its value. Such cases were defined to be edge-objects and removed from the list.

3.2 Spectral extraction

The light profile of each object as imaged with the *HST F775W* filter was modelled with a 2D-Gaussian. (That is, effectively, the *HST* imaging data was used to provide us with a prior on the shape of the object.) For any given target field, the MUSE Point Spread function (PSF) was fit using bright stars where these were available. Where not, a number of these 2D-Gaussian galaxy models (around ten per field) were convolved with a varying set of Gaussians, and the results were subtracted from the MUSE images of the same galaxies. The best-fitting (smallest residual) Gaussian function was taken to be the PSF. The procedure was carried out over several spectral bins of the MUSE data cube to derive the wavelength dependence of the PSF. (Further details on the PSF estimation are found in Herenz et al. 2017.)

Following this PSF estimation for each field, each 2D-Gaussian galaxy model was analytically convolved with the wavelength-dependent 2D-Gaussian model of the PSF. The resulting MUSE

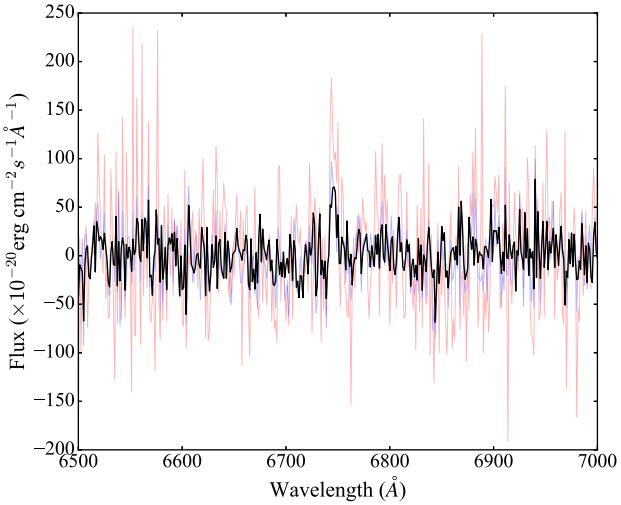

Figure 1. The spectrum shown in black has been optimally extracted as described in Section 3.2, whereas circular aperture extractions with radii of 10 and 5 pixels are shown in red and blue, respectively. The optimal extraction improves the S/N as it downweights noisier pixels in the outer regions of the aperture. The suppression of noisy spikes in the spectra greatly facilitates visual searches for Ly α.

PSF-convolved template was then used to optimally extract the spectra, where (following directly from the least-squares condition applied to the template matching problem), the flux in spectral layer k is given by

$$\alpha_k = \frac{\sum_{ij}\left[(d_{ijk} \times t_{ijk})/\sigma^2_{ijk}\right]}{\sum_{ij}\left[t^2_{ijk}/\sigma^2_{ijk}\right]}, \quad (1)$$

where d_{ijk}, t_{ijk} and σ_{ijk} denote, respectively, the value of the data, template and standard deviation ($\sqrt{var}$) at the voxel with coordinates i, j, k. An example spectrum extracted via this method is shown in Fig. 1. The spectra that were extracted via this method were then searched for Ly α emission but were not used for flux measurements since while they exhibit an improved signal-to-noise ratio (S/N), the total flux can be biased.

3.3 Assembling the Ly α catalogue

To assemble our catalogue of Ly α emitters we used a data product from the software LSDCAT[1] (Herenz & Wisotzki 2017) to facilitate the search for emission lines in our spectra. LSDCAT is a tool that was developed to find line emitters that lack a continuum detection in MUSE data cubes. Whilst we did not make use of LSDCAT's line-emitter cataloguing function, as we are here interested in sources that *do* exhibit continuum emission in the *HST* images (and, for the brighter objects, the MUSE cubes), one of its data products was useful for our analysis, as we describe next.

The premise of LSDCAT is based on matched-filtering, whereby the data cubes are cross-correlated with a template that represents an expected emission line's 3D profile, thus maximizing the S/N of faint emission lines. One of its data products is an S/N cube, every voxel of which represents the S/N of the respective voxel in a MUSE data cube. An S/N spectrum from this S/N cube was extracted at the centre-coordinates of each source in our continuum-bright-selected catalogue. We inspected this S/N spectrum to search for features with S/N $>$ 4, and the wavelength at which such peaks occurred was recorded. Following this, for each recorded spectral feature, we ran a search for a higher S/N peak in surrounding voxels in the cube (namely, within a circular radius of 3 voxels spatially and 1 voxel spectrally). The reason for this procedure is to (1) account for any discrepancies in astrometry, and (2) take into account the possibility that peak Ly α emission may occur in a voxel that is spatially offset from the centre coordinates based on the continuum image (at which coordinates the S/N spectrum had been extracted), and which therefore might also exhibit a corresponding slight shift in the spectral direction. Where this routine returned a higher S/N peak in a surrounding voxel, the spatial and spectral coordinates of this peak were recorded for that particular feature.

The spectral resolution of MUSE is sufficient to resolve the separate components of the [O II] doublet, which greatly reduces the possibility of mistaking [O II] for Ly α. We visually inspected the spectral features in the (non-smoothened) optimally-extracted spectra. We also inspected the shape of the spectral features following a simple, circular, varying-size aperture extraction to further guard against mistaking artefacts for genuine emitters. As a final check, for each spectral feature, we also inspected the layer in the cube where the peak of the spectral feature occurred. A cosmic-ray hit or other artefact would, in general, be expected to exhibit a very narrow spatial extent and is easier to flag in a 2D cube layer. In the end, following this visual inspection, for our final Ly α catalogue, we utilized an S/N cut of 5.0, as this was determined to securely guard against artefacts. Following further work on assessing the MUSE data cubes' noise properties, it was found that the effective noise was initially underestimated by a factor of 1.2, which effectively means that our S/N = 5.0 cut actually corresponds to S/N $\approx$ 4.0, and we are able to distinguish real emitters from artefacts at this lower S/N level. Ly α emission was securely detected in 100 sources in our sample.

3.4 Redshift determination

We define the Ly α emitter fraction, $X_{\mathrm{Ly}\,\alpha}$ as

$$X_{\mathrm{Ly}\,\alpha} = \frac{\textit{HST}\text{ continuum-detected sources exhibiting Ly}\,\alpha}{\textit{HST}\text{ continuum-detected sources}} \quad (2)$$

Prior to making any further use of the photometric redshifts – essential for the determination of the denominator in equation (2) – we applied a redshift correction, the motivation for which is described below.

Following the identification of Ly α emitters in our sample, we investigated the relation between photometric redshift and spectroscopic redshift for the entire Ly α sample, as shown in Fig. 2. As is evident from this figure, with the exception of 10 objects, all sources exhibit a spectroscopic redshift that is slightly higher than the corresponding photometric redshift found by Skelton et al. (2014), an effect that is also visible in Fig. 23 of the same paper for this redshift range. Oyarzún et al. (2016) found that the magnitude of this offset correlates with Ly α EW, so a possible source for this discrepancy could be due to the Ly α emission line altering the photometry, an effect that is not accounted for in the photo-z spectral energy distribution templates (see Schaerer & de Barros 2012). A detailed investigation of this systematic offset between photometric and spectroscopic redshifts will be presented in Brinchmann et al. (submitted), where the role of the applied intergalactic absorption model and the effect of spatially overlapping galaxies are also explored.

[1] The source code is available in Herenz & Wisotzki (2016).

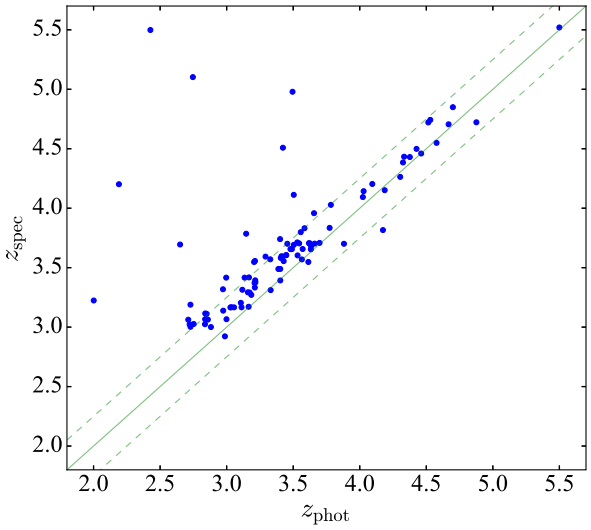

Figure 2. Spectroscopic redshift versus photometric redshift. The two dashed lines correspond to $|z_{\rm spec} - z_{\rm phot}| = 0.25$. The average difference between $z_{\rm spec}$ and $z_{\rm phot}$ of 0.1 ($\pm$0.01) was used as a correction factor for the photometric redshifts.

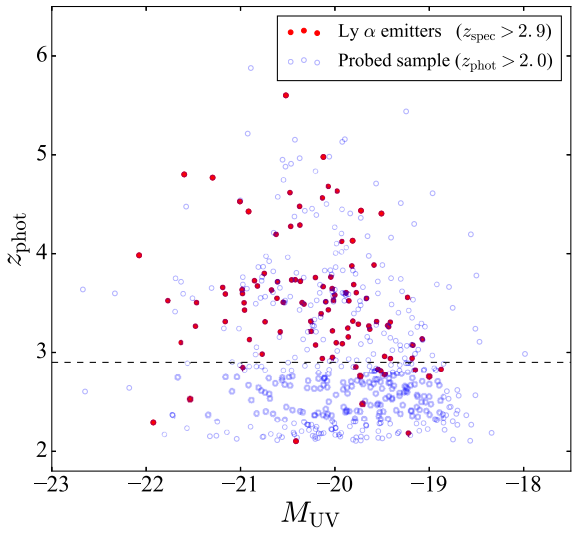

Figure 3. The sample of 100 Ly α emitting galaxies (red) amongst the entire sample of 532 continuum-selected objects with $z_{\rm phot} > 2.0$ (open blue circles). The dashed horizontal line marks $z = 2.9$, the redshift at which Ly α enters the MUSE redshift window.

Ignoring outliers on this plot, where by outliers we mean sources for which $|z_{\rm spec} - z_{\rm phot}| > 0.25$ (represented in Fig. 2 by two dashed lines), we calculate the required redshift correction, calculated as the mean of the difference between $z_{\rm phot}$ and $z_{\rm spec}$ for each Ly α emitter:

$$\text{Redshift correction} = \frac{1}{N}\sum_{i}^{N}(z_{\rm phot_i} - z_{\rm spec_i}), \quad (3)$$

where N denotes the total number of Ly α emitters and i is an individual emitter. We find this redshift correction to be 0.10 ($\pm$0.01). We correct the photometric redshift of the entire sample of 532 objects. Out of 198 continuum sources with $z_{\rm phot}$ (or $z_{\rm spec}$ where available) $>$2.9 (which is the redshift at which Ly α enters the MUSE redshift range) and $-22.5 < M_{\rm UV} < -18.5$, we find Ly α emission in 100 sources (see Fig. 3).

3.5 Flux measurements

The LSDCAT routine `lsd_cat_measure.py` was used to measure the fluxes of the Ly α lines. This routine creates a 'pseudo-narrow' band image from the data cube centred on the emission line. The bandwidth of this image is defined by the spectral layers in which the emission line is above a certain analysis threshold $S/N_{\rm ana.}$ in the S/N cube. By visual inspection (separate from that described in Section 3.3), we found that $S/N_{\rm ana.} = 4$ separates the emission line signal from the noise. The flux is then integrated in these narrow-band images within $3 \times R_{\rm Kron}$ apertures, where $R_{\rm Kron}$ is the characteristic light distribution weighted radius introduced by Kron (1980), centred on the first central-moment calculated in a PSF-smoothed version of the pseudo-narrow image. In the vast majority of cases, LSDCAT's automatic line flux measurements agree well with fluxes determined from a manual curve-of-growth analysis (Herenz & Wisotzki 2017).

3.6 EW measurements

For most sources, the 1 h integration time with MUSE was not sufficient to detect the continuum directly from the extracted MUSE spectra, so we used *HST* ACS imaging in the *F*814*W* band to obtain the continuum flux density for our sources. The *F*814*W* band is the deepest *HST* band for CANDELS CDFS and therefore best suited for this purpose. Whilst Ly α enters the redshift window of the *F*814*W* band at $z = 4.97$–6.23, we note that only four objects in the entire Ly α sample lie in this redshift range. Moreover, even in such cases, Ly α contamination is not expected to have any significant effect on the *F*814*W* magnitude since (a) the galaxies are selected to be continuum-bright, and (b) the scalelength of Ly α is much larger than the size of the aperture used for *HST* flux measurements, meaning that much of the Ly α emission is excluded. Therefore, any subtraction of the Ly α flux from the *F*814*W* magnitude would almost certainly result in over-subtraction.

We used GALFIT (Peng et al. 2010) to fit each of our objects with Sérsic profiles to optimally determine their magnitudes. In converting the magnitude into continuum flux density at the position of the Ly α line, we assumed a continuum slope with a mean $\beta = -2$ (e.g. Ouchi et al. 2008, Blanc et al. 2011, Castellano et al. 2014). From this measure of the continuum and the line flux measurements obtained directly from the MUSE data cubes (via LSDCAT), we computed the EWs for our sources.

Traditionally, both the line flux and the continuum flux are measured in the same fixed aperture. This, however, is not optimal because there is evidence that Ly α emission is more extended than the UV continuum (Momose et al. 2016; Wisotzki et al. 2016; Xue et al. 2017). This would necessitate the use of larger apertures for the line flux measurements. However, two problems would arise if one were to use the same larger aperture to also obtain a measurement of the continuum flux density. First, the noise would increase and, secondly, the large size of the aperture could potentially include other sources (e.g. low-redshift interlopers). Therefore, taking advantage of the deep broad-band data and deriving individual fits for objects is the best approach for the present sample of Ly α emitting galaxies.

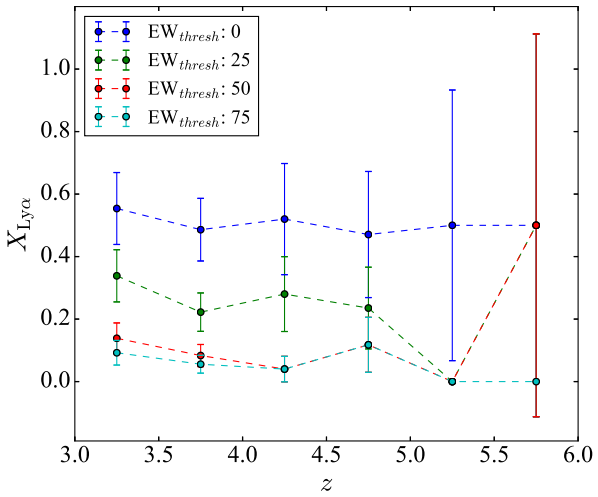

Figure 4. $X_{Ly\,\alpha}$ versus redshift for different rest-EW thresholds. The error bars are derived via error-propagation of Poissonian statistics, such that $\sigma = (N_{Ly\alpha}/N_z^2 + N_{Ly\alpha}^2/N_z^3)^{1/2}$, where $N_{Ly\alpha}$ is the number of Ly α emitters within a given redshift bin and N_z is the number of continuum sources in the same bin.

4 RESULTS AND DISCUSSION

The final set of Ly α emitting galaxies consists of 100 objects spanning $z = 2.92$–5.52 (see Table A1).

Considering Fig. 4, which focuses on $3.0 < z < 6.0$,[2] we find $X_{Ly\,\alpha} \approx 0.5$ or larger over this redshift range when the entire sample of Ly α emitters is considered (see also Table 1). We further consider $X_{Ly\,\alpha}$ for three rest-EW cuts: 25, 50, and 75 Å. Comparing with previous studies, we note that Cassata et al. (2015) find $X_{Ly\,\alpha} \approx 0.12$ over $z = 3$–4 for rest-EW >25 Å. For the same EW cut, we find $X_{Ly\,\alpha} \geq 0.22$, a two-fold increase in the fraction of Ly α emitters in this same redshift range.

We investigated the variation of $X_{Ly\,\alpha}$ with z, adopting Poissonian statistics for our error bars such that the propagated error for $X_{Ly\,\alpha}$ is $\sigma = (N_{Ly\alpha}/N_z^2 + N_{Ly\alpha}^2/N_z^3)^{1/2}$. Formalizing our null hypothesis to state that there is no correlation between $X_{Ly\,\alpha}$ and z, we perform weighted least squares regression on the data for each rest-EW cut, and derive F-test p-values of 0.13 (0Å), 0.39 (25Å), 0.22 (50Å) and 0.35 (75Å), all falling short of the 95 per cent confidence level ($p = 0.05$). Therefore, even adopting this simplified (propagation of $\sqrt{N}$ error) approach, we fail to reject the null hypothesis, discerning no dependence of $X_{Ly\,\alpha}$ on z regardless of the EW cut adopted. While data points at $z > 5$ have relatively large uncertainties, potentially obscuring an underlying trend of increasing $X_{Ly\,\alpha}$, no dependence of $X_{Ly\,\alpha}$ on z is observed at $z < 5.0$ either. At any rate, this exercise suggests that any underlying trend cannot be particularly strong.

We also investigated any potential trends of $X_{Ly\,\alpha}$ with UV luminosity, again adopting the same rest-EW cuts and employing the above analysis, finding $p = 0.46$ (0Å), 0.04 (25Å), 0.37 (50Å) and 0.27 (75Å). Some previous studies note a trend of a rising $X_{Ly\,\alpha}$ with fainter UV luminosity (e.g. Stark et al. 2010 for $z = 3.5$–6). However, as shown in Fig. 5a, our first MUSE-Wide results do not seem to indicate any overall significant correlation between the two quantities except marginally for the case with a rest-EW cut of 25Å (p = 0.04), thus being more in line with the findings of Cassata et al. (2015), who also do not find such a relationship. It will be interesting to explore in subsequent studies whether a larger sample will reveal any dependence of $X_{Ly\,\alpha}$ on M_{UV}.

29 per cent of the Ly α sample exhibits rest-EWs $\leq$ 15 Å. We should note that our sample is S/N-limited, which effectively translates into it being flux-limited at a given redshift. The S/N provided by LSDCAT is dependent on the compact Ly α flux, which may be (albeit not necessarily) smaller than the total flux. This is attributable to there being: (a) a range of halo sizes and line-widths, and (b) an error on the flux measurement itself. Effectively, this means that a given S/N value corresponds to a range of measured fluxes. For a continuum magnitude-defined sample, this flux limit (picked arbitrarily from the selection function at 50 per cent completeness; see Herenz et al., in preparation, for details) can be converted into an EW limit. Across the redshift range explored by our data, we find median rest-EW limits of 30.36 ($z = 3.0$–3.5), 27.86 ($z = 3.5$–4.0), 25.63 ($z = 4.0$–4.5), 23.22 ($z = 4.5$–5.0), 35.19 ($z = 5.0$–5.5) and 37.73 ($z = 5.5$–6.0), with the overall median rest-EW in the $z = 3.0$–5.5 range being 27.86 Å. Such a limit, however, is strongly dependent on the continuum magnitude. This, in fact, explains the existence of very low EW emitters in our sample – smaller even than what one would otherwise expect; even a small EW emitter will be detected if the source has a bright enough continuum. The probing of $\lesssim$ 10 Å EWs highlights the excellent capability of MUSE to detect low rest-EW sources with relatively short (i.e. 1 h) integration times. By adding sensitivity to the low-EW regime, even 'shallow' surveys with MUSE can provide new insight into the size of the overall fraction of Ly α emitters.

This work also raises the possibility of implications for higher redshift observations. Presently, various studies in the literature observe a drop in $X_{Ly\,\alpha}$ at higher redshifts (e.g. Treu et al. 2013, Caruana et al. 2014, Tilvi et al. 2014). Given the flat trend of $X_{Ly\,\alpha}$ with redshift observed in this study, such a result could suggest that there might be a significant component of extended Ly α residing in the haloes surrounding these sources (see also Wisotzki et al. 2016), which could have been missed by previous studies utilizing slit spectroscopy by virtue of the slit not being large enough to encompass this emission. Furthermore, since Ly α emission with a high rest-EW seems to be more readily observable amongst fainter galaxies (Fig. 5b), the search for this line might be more fruitful were one to look at fainter objects rather than targeting the brighter galaxies. However, at present, this remains an open question; if the Universe has a significant HI neutral fraction at $z > 6$, then lower-luminosity galaxies might not be able to ionize a sufficiently large HII bubble around them, which would result in stronger attenuation of Ly α in these fainter systems.

This study illustrates that MUSE can probe low EW emitters at redshifts up to $z \approx 5$ with relatively short integration times. With integrations of the order of 1 h, we are able to probe sub–10 Å EWs – and can detect Ly α emitters with rest-EW >10 Å, constituting $\approx$ 80 per cent of our sample, with high confidence.

[2] By virtue of the redshift range selected (which allows for straightforwardly-cut redshift bins), this figure omits 5 emitters with $2.9 < z < 3.0$.

ACKNOWLEDGEMENTS

This research is based on observations collected at the European Organization for Astronomical Research in the Southern hemisphere under ESO programme 094.A-0205(B).

We thank the anonymous referee whose helpful comments greatly improved this manuscript.

We acknowledge funding by the Competitive Fund of the Leibniz Association through grants SAW-2013-AIP-4 and SAW-2015-AIP-2. This work is supported by Fundação para a Ciência e a Tecnologia (FCT) through national funds

Table 1. The Ly α fraction per redshift bin. In each case, the numerator denotes the number of sources exhibiting Ly α emission within a given redshift bin, whereas the denominator denotes the number of continuum sources in the same bin. These fractions are represented in Fig. 4.

	$3.0 < z < 3.5$	$3.5 < z < 4.0$	$4.0 < z < 4.5$	$4.5 < z < 5.0$	$5.0 < z < 5.5$	$5.5 < z < 6.0$
$EW_{thresh} = 0$Å	36/65	35/72	13/25	8/17	2/4	1/2
$EW_{thresh} = 25$Å	22/65	16/72	7/25	4/17	0/4	1/2
$EW_{thresh} = 50$Å	9/65	6/72	1/25	2/17	0/4	1/2
$EW_{thresh} = 75$Å	6/65	4/72	1/25	2/17	0/4	0/2

Table 2. The Ly α fraction per magnitude bin. In each case, the numerator denotes the number of sources exhibiting Lyα emission within a given M_{UV} bin, whereas the denominator denotes the total number of continuum sources in that bin. These fractions are represented in Fig. 5a.

	$-22.5 < M_{UV} < -21.5$	$-21.5 < M_{UV} < -20.5$	$-20.5 < M_{UV} < -19.5$	$-19.5 < M_{UV} < -18.5$
$EW_{thresh} = 0$Å	6/12	26/56	54/102	14/28
$EW_{thresh} = 25$Å	1/12	13/56	29/102	10/28
$EW_{thresh} = 50$Å	1/12	4/56	9/102	6/28
$EW_{thresh} = 75$Å	1/12	2/56	7/102	4/28

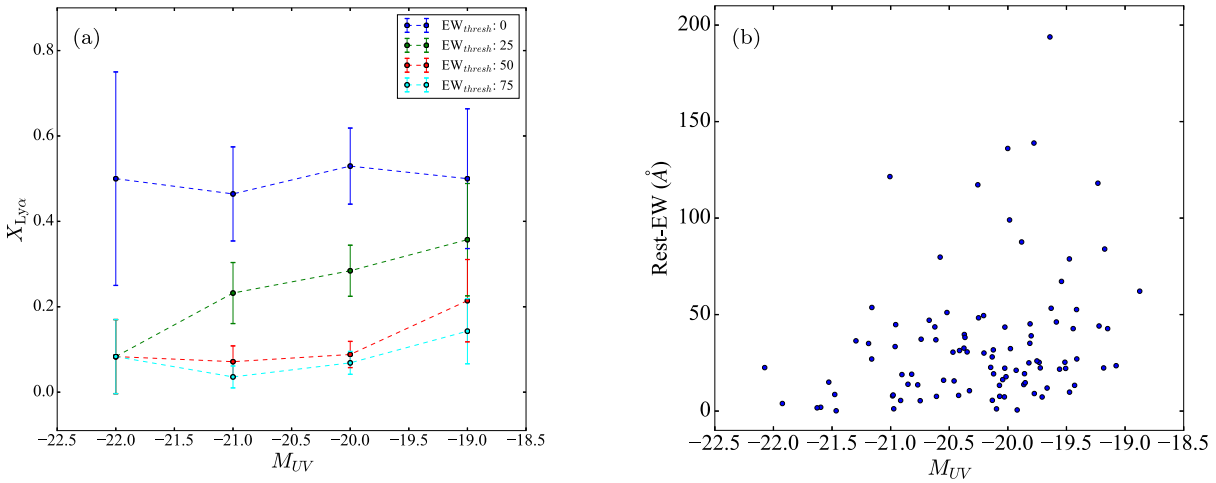

Figure 5. $X_{Ly\alpha}$ versus UV luminosity and rest-EW versus M_{UV}. (a) $X_{Ly\alpha}$ versus UV luminosity for various rest-EW cuts. We find no evidence of a correlation between the two quantities for any of the rest-EW cuts adopted. The error bars are derived via error-propagation of Poissonian statistics, such that $\sigma = (N_{Ly\alpha}/N^2_{M_{UV}} + N^2_{Ly\alpha}/N^3_{M_{UV}})^{1/2}$, where $N_{Ly\alpha}$ is the number of Ly α emitters within a given M_{UV} bin, and $N_{M_{UV}}$ is the total number of continuum sources in the same bin. (b) Rest-EW versus M_{UV}. There is a smaller number of bright ($M_{UV} \lesssim -21.0$) objects with moderate to high Ly α EWs. [Note that this figure omits three outlying sources with very large rest-EWs (366Å, 633Å and 1118Å at $M_{UV} = -20.48$, -21.77 and -19.01, respectively) in order to aid better viewing of the rest of the sample.]

(UID/FIS/04434/2013) and by FEDER through COMPETE2020 (POCI-01-0145-FEDER-007672). During part of this work, JB was supported by FCT through Investigador FCT contract IF/01654/2014/CP1215/CT0003. RAM acknowledges support by the Swiss National Science Foundation. JS acknowledges ERC Grant agreement 278594-GasAroundGalaxies. TG is grateful to the LABEX Lyon Institute of Origins (ANR-10-LABX-0066) of the Université de Lyon for its financial support within the program 'Investissements d'Avenir'(ANR-11-IDEX-0007) of the French government operated by the National Research Agency (ANR).

REFERENCES

Amorín R. et al., 2017, Nature, 1, 52
Bacon R. et al., 2010, in McLean I. S., Ramsay S. K., Takami H., eds, Proc. SPIE Conf. Ser. Vol. 7735. Astronomical Telescopes & Instrumentation. SPIE, Bellingham, p. 773508
Blanc G. et al., 2011, ApJ, 736, 31
Brammer G. B. et al., 2012, ApJS, 200, 13
Caruana J., Bunker A. J., Wilkins S. M., Stanway E. R., Lacy M., Jarvis M. J., Lorenzoni S., Hickey S., 2012, MNRAS, 427, 3055
Caruana J., Bunker A. J., Wilkins S. M., Stanway E. R., Lorenzoni S., Jarvis M. J., Ebert H., 2014, MNRAS, 443, 2831
Cassata P. et al., 2015, A&A, 573, 24
Castellano M. et al., 2014, A&A, 566, A19
Dayal P., Maselli A., Ferrara A., 2011, MNRAS, 410, 830
Dijkstra M., 2014, Publ. Astron. Soc. Aust., 31, e040
Forero-Romero J. E., Yepes G., Gottlober S., Prada F., 2011, MNRAS, 419, 952
Garel T., Blaizot J., Guideroni B., Michel-Dansac L., Hayes M., Verhamme A., 2015, MNRAS, 450, 1279
Garel T., Guideroni B., Blaizot J., 2016, MNRAS, 455, 3436
Giavalisco M. et al., 2004, ApJ, 600, 93
Grogin N. A. et al., 2011, ApJS, 197, 35
Guo Y. et al., 2013, ApJ, 207, 24

Herenz E. C., Wisotzki L., 2016, ASCL, available at: http://adsabs.harvard.edu/abs/2016ascl.soft12002H
Herenz E. C., Wisotzki L., 2017, A&A, 602, A111
Herenz E. C. et al., 2017, A&A, in press
Kakiichi K., Dijkstra M., Ciardi B., Graziani L., 2016, MNRAS, 463, 4019
Koekemoer A. M. et al., 2011, ApJS, 197, 36
Kron R. G., 1980 ApJS, 43, 305
Mallery R. P. et al., 2012, ApJ, 760, 128
Momcheva I. G. et al., 2016, ApJS, 225, 27
Momose R. et al., 2016, MNRAS, 457, 2318
Oke J. B., Gunn J. E., 1983, ApJ, 266, 713
Ono Y. et al., 2012, ApJ, 744, 83
Ouchi M. et al., 2008, ApJS, 176, 301
Oyarzún et al., 2016, ApJ, 821, L14
Peebles P. J. E., Partridge R. B., 1967, ApJ, 148, 713
Peng C. Y., Ho L. C., Impey C. D., Rix H. W., 2010, AJ, 139, 2097
Pentericci L. et al., 2011, ApJ, 743, 132
Rhoads J. E., Malhotra S., Dey A., Stern D., Spinrad H., Jannuzi B. T., 2000, ApJ, 545, L85
Schaerer D., de Barros S., 2012, in Tuffs R. J. and Popescu, C. C., eds, Proc. IAU Symp. 284, The Spectral Energy Distribution of Galaxies - SED 2011. Kluwer, Dordrecht, p. 20
Schenker M. A., Stark D. P., Ellis R. S., Robertson B. E., Dunlop J. S., McLure R. J., Kneib J.-P., Richard J., 2012, ApJ, 744, 179
Skelton R. E. et al., 2014, ApJS, 214, 24
Stark D. P., Ellis R. S., Chiu K., Masami O., Bunker A., 2010, MNRAS, 408, 1628
Tilvi V. et al., 2014, ApJ, 794, 5
Treu T. Schmidt K. B., Trenti M., Bradley L. D., Stiavelli M., 2013, ApJ, 775, 29
Wisotzki L. et al., 2016, A&A, 587, 98
Xue R. et al., 2017, ApJ, 837, 172

APPENDIX: THE LY α CATALOG

Table A1. The catalog of Ly α emitters.

ID (Skelton)	ID (Guo)	M_{UV} ($F814W$)	Flux [3-Kron] ($\times 10^{-20}$ erg cm^{-2} s^{-1})	Flux σ ($\times 10^{-20}$ erg cm^{-2} s^{-1})	rest-EW (Å)	rest-EW σ (Å)	z
18198	8932	− 21.77	114164.98	338.13	632.61	15.4	4.51
18702	9262	− 20.9	4988.66	452.38	18.91	1.87	3.17
18439	9093	− 20.74	3262.53	341.16	37.24	3.91	3.37
14173	6905	− 20.75	680.32	184.99	5.38	1.46	3.71
7781	4229	− 20.58	9534.21	601.57	79.76	6.95	3.2
23859	12329	− 21.16	10591.73	574.63	53.67	2.95	3.66
22379	11427	− 20.26	12063.1	548.33	117.24	5.44	3.39
18974	9435	− 20.82	3059.63	354.4	19.09	2.36	3.66
21324	10812	− 20.67	6175.14	460.42	47.06	3.61	3.71
25614	13375	− 21.6	249.07	113.65	1.96	0.89	4.85
20768	10433	− 21.46	42.13	2256.53	0.15	7.91	3.49
13283	6531	− 22.07	4565.68	375.97	22.52	1.94	3.7
11864	5783	− 20.98	1497.97	243.61	7.86	1.3	3.6
12589	6235	− 20.55	2100.37	192.16	15.98	1.55	3.58
15002	7233	− 20.85	1637.24	289.11	13.9	2.91	3.7
14982	7259	− 21.48	3425.0	423.31	8.59	1.07	3.17
17777	8701	− 21.16	6895.07	458.29	26.98	2.11	3.33
16007	7775	− 20.91	654.41	158.68	5.49	1.33	4.38
15158	7350	− 20.35	3196.17	359.63	30.65	3.53	3.39
16710	8108	− 20.77	3532.28	340.15	13.59	1.71	3.0
18517	9113	− 20.42	884.34	201.51	8.12	1.85	3.68
17484	8544	− 20.96	1316.61	247.48	33.42	6.31	3.74
15419	7464	− 21.92	380.46	137.68	3.92	1.46	4.2
16523	8005	− 21.19	6613.16	307.01	35.04	2.0	3.8
16492	7986	− 21.3	2031.47	221.07	36.38	4.02	4.71
17539	8584	− 20.61	5504.49	325.41	36.93	3.52	3.61
18429	9060	− 20.96	6883.15	329.17	44.79	2.43	3.57
18384	9109	− 21.63	1126.04	294.31	1.67	0.51	3.07
18841	9317	− 20.61	988.01	1802.64	7.61	13.89	3.55
19906	9945	− 21.01	8841.52	356.03	121.5	9.24	4.5
21106	10675	− 20.37	1985.24	285.89	32.62	4.74	4.43
20804	10491	− 20.04	1307.61	254.49	16.29	3.33	3.7
21734	11040	− 20.07	642.29	141.26	13.33	3.0	4.55
23169	11909	− 20.12	1029.91	179.07	19.3	3.97	4.72
15660	7587	− 19.73	2118.74	365.79	25.25	4.37	2.98
12277	6113	− 19.86	739.76	2162.86	13.73	40.16	3.79
12145	6060	− 19.82	1036.77	227.71	24.98	5.55	3.83
14405	6983	− 19.77	417.6	114.95	9.08	2.51	4.11
13558	6622	− 19.59	1778.54	234.15	46.16	6.31	4.03
13253	6490	− 19.18	1233.8	1810.08	22.35	32.79	3.11
10447	5354	− 19.8	2096.78	315.5	39.0	5.94	3.83
10849	5504	− 19.22	1234.62	234.96	44.08	8.63	2.98
22284	11369	− 20.41	3032.79	387.22	31.36	4.01	3.22

Table A1 – *continued*

ID (Skelton)	ID (Guo)	M_{UV} ($F814W$)	Flux [3-Kron] ($\times 10^{-20}$ erg cm^{-2} s^{-1})	Flux σ ($\times 10^{-20}$ erg cm^{-2} s^{-1})	rest-EW (Å)	rest-EW σ (Å)	z
23895	12341	– 20.0	10591.73	574.63	136.07	7.49	3.66
23150	11872	– 20.21	2101.3	238.72	49.48	6.3	3.96
23881	12313	– 20.48	10591.73	574.63	365.81	28.33	4.72
20679	10410	– 20.02	1291.02	214.98	17.79	3.0	3.56
18978	9384	– 19.56	1141.04	207.66	21.71	4.0	3.56
15549	7493	– 20.98	– 3548.04	2679.83	8.32	3.95	4.98
19097	9462	– 20.25	3904.14	453.15	48.32	6.21	3.17
16981	8268	– 20.13	1208.13	201.57	28.06	4.69	4.46
15294	7416	– 20.15	2454.19	264.42	22.64	2.62	3.59
15815	7663	– 20.37	2812.89	322.6	39.68	5.28	4.15
15601	7570	– 19.75	1901.85	305.7	25.97	4.18	3.27
14421	7043	– 19.86	1133.53	215.89	19.36	3.71	3.17
13851	6766	– 19.81	1945.14	291.95	45.18	6.83	3.38
14403	7004	– 19.08	1145.76	214.62	23.51	4.99	3.17
14204	6920	– 19.98	1229.0	257.03	32.35	6.97	4.74
11528	5787	– 20.37	3104.33	380.56	38.16	6.32	3.71
9990	5164	– 19.99	6221.49	574.65	99.03	9.85	3.42
9553	5004	– 19.63	3703.81	401.12	53.27	5.85	3.42
8885	4733	– 19.81	2507.22	325.77	35.11	32.74	4.14
23111	11857	– 20.62	3949.69	411.04	43.61	4.72	4.2
13755	6717	– 19.41	1641.82	332.96	27.01	5.57	3.02
15282	7400	– 19.47	714.8	251.45	9.82	3.53	3.06
15632	7566	– 19.67	746.34	240.56	11.94	3.86	3.61
9596	5026	– 19.78	9309.24	596.16	138.88	8.99	3.03
11404	5746	– 20.1	100.9	1932.33	1.14	21.74	3.6
12704	6280	– 20.03	1941.63	292.62	22.22	3.81	3.31
11074	5616	– 20.03	560.66	213.62	7.34	2.8	3.7
9766	5096	– 19.43	971.32	219.52	13.33	3.74	3.29
11592	5833	– 19.85	685.39	163.08	14.68	3.5	3.59
12439	6184	– 19.88	5841.01	444.68	87.62	6.72	3.69
11127	5628	– 18.88	2367.73	315.82	62.12	12.78	3.19
12575	6234	– 19.01	25349.49	833.42	1117.86	119.07	3.69
11328	5665	– 20.47	914.45	1559.4	30.53	52.07	3.82
11149	5645	– 20.03	3232.13	391.39	43.51	5.6	3.11
14891	7207	– 21.53	701.74	146.73	14.99	3.42	5.5
10699	5447	– 19.71	778.12	290.28	7.29	3.86	2.99
13365	6526	– 19.51	1424.6	301.88	25.31	5.44	3.06
14541	29103	– 19.23	5399.7	417.07	118.07	9.6	3.7
13084	6433	– 19.92	66.4	180.43	0.58	1.58	2.92
13532	6616	– 19.15	1856.91	284.91	42.72	7.73	3.02
15546	7538	– 20.52	2299.63	348.04	51.07	9.25	5.52
16198	7847	– 20.2	2190.42	317.52	30.07	4.37	3.14
14809	7154	– 20.46	1705.43	218.19	15.62	2.18	3.65
15130	7304	– 20.97	96.06	128.01	1.17	1.56	5.1
14703	7151	– 19.93	1089.17	197.41	21.13	6.35	4.09
17385	8493	– 20.13	440.18	180.15	5.57	3.03	3.07
17741	8702	– 20.07	1556.26	247.15	7.65	2.88	3.31
16269	7896	– 19.17	3341.44	300.64	83.96	7.9	3.32
18872	9340	– 19.48	4635.43	412.64	78.83	7.05	3.0
19538	9735	– 19.51	836.4	151.79	22.1	4.7	4.26
17356	8485	– 19.54	5972.33	488.59	67.19	5.63	3.0
17612	8621	– 19.44	3032.74	320.9	42.72	5.48	3.29
16398	7947	– 20.33	1108.53	201.67	10.54	1.93	3.49
18576	29778	– 19.72	454.82	178.97	22.37	8.86	4.43
19390	9653	– 20.12	2314.72	266.92	31.71	3.84	3.57
19717	9858	– 19.64	7681.29	451.84	193.86	13.46	3.42
18773	9266	– 19.41	1715.65	255.01	52.61	8.06	3.55

This paper has been typeset from a TEX/LATEX file prepared by the author.